Evaluating unsteady fluid dynamic forces in viscous flows from the vorticity field

Juan Li * and Yinan Wang †
The University of Warwick, Coventry, CV4 7AL, U.K.

Michael Graham‡
Imperial College, London, SW7 2BY, U.K.

Xiaowei Zhao §
The University of Warwick, Coventry, CV4 7AL, U.K.

The vortex force map (VFM) method is a promising low-cost technique for predicting unsteady aerodynamic load from the vorticity field. Developed under potential flow assumption and applied to high-resolution computational fluid dynamics (CFD) data, the original VFM method needs to be further explored for viscous flows, especially at low Reynolds numbers and with incomplete knowledge of the flow data. In this paper the VFM method is extended to general viscous flows, with both forces contributed from vorticity in the flow field and on the body surface considered. We find that viscosity contributes to not only the skin friction force but also a pressure force term. We also show that the extended vortex pressure force maps for general flow problems without the potential flow assumption lead to vanishing contributions from the far field. The extended VFM method is applied to CFD flow fields for the starting flow of a cylinder and an NACA0012 airfoil, and it is used to analyze the force contribution effect of a given vortex. Moreover, acceptable accuracy of the method on truncated domains and under coarse sampling of typical particle image velocimetry (PIV) measurement size is demonstrated.

Nomenclature

(Nomenclature entries should have the units identified)

ℓ_B = characteristic length of the body

c_A = chord length of the airfoil

a = radius of the cylinder

x, y = coordinates in body fixed frame

*Marie-Curie Early Stage Researcher, School of Engineering
†Research Fellow, School of Engineering
‡Professor, Department of Aeronautics
§Professor, School of Engineering; xiaowei.zhao@warwick.ac.uk (Corresponding Author)

τ = non-dimensional time

L = lift

D = drag

C_L = lift coefficient

C_D = drag coefficient

P = pressure field

ρ = density

μ = viscosity

Ω_B = the volume occupied by solid body

S_B = the surface of the solid body in three dimensions

l_B = the surface of the solid body in two dimensions

$\overrightarrow{n_B}$ = the normal vector pointing inward from the body surface

Ω = the control volume (occupied by fluid)

S_∞ = the outer boundary of the control volume

V_∞ = free stream velocity

α = angle of attack

$\overrightarrow{U}$ = velocity distribution of the flow field

$\overrightarrow{\omega}$ = vorticity distribution of the flow field

$\overrightarrow{F}$ = total force acting on the body

ϕ_k^* = the velocity potential induced by unit incident velocity of ideal flow in the k^{th}-direction

ϕ_k = the velocity potential induced by the translational motion of Ω_B at unit speed in the k^{th}-direction

$\overrightarrow{\Lambda}_k$ = vortex force vector

Subscripts

N = normal component

A = axial component

g = ground-fixed frame

k = index of directions

Superscripts

add = added mass force term

vp = vortex pressure force term

vis-p = viscous pressure force term

vis-f = skin friction force term

I. Introduction

Unsteady force approaches are important in revealing the mechanisms behind a range of vortex-dominated natural flows, including flapping wings for birds [1] and insects [2], rotating wings of seeds [3] and fish locomotion [4]. Force approaches which relate the aerodynamic/hydrodynamic forces to flow structures (e.g. vortices) are also helpful in drag reduction [5], thrust generation [5], high lift strategies [6] and load alleviation [7] through active or passive controls in artificial flows.

For predicting the unsteady force acting on the body in separated flows, a detailed knowledge of the entire vorticity field is normally required and few analytical methods are available. More success has been made with analytical-numerical coupling methods. These include unsteady thin airfoil theory corrected by additional vortices [8–10] or the use of the unsteady Blasius equation [11] to calculate the forces. On the other hand, accurate experimental measurements on fluid dynamic loads in separated flows are possible with the development of high-precision experimental techniques [8]. However such direct load measurements are not always easy to execute for flow problems at low Reynolds numbers, as the fluid dynamic loads tend to be very small and are subject to significant measurement errors [12]. Moreover, direct load measurements can be significantly contaminated by resonance effect. Meanwhile, obtaining fluid dynamic loads from an integration of computed surface pressures and skin friction, the normal method used in computational fluid dynamics (CFD), has its difficulties since resolving the entire boundary layer to an adequate resolution near the solid surface in unsteady particle image velocimetry (PIV) data is far more difficult than in CFD simulations [12]. As a result, volumetric pressure-free methods have seen development for the purpose of taking advantage of accurate experimental measurements of flow fields such as PIV, and extracting the force on the body in a non-intrusive way. This also helps in providing a better insight into the specific influence of each individual flow structure on the force.

Volumetric pressure-free methods date back to Milne-Thomson [13], who expressed the total momentum of an incompressible flow in a domain as the moment of the hydrodynamic impulse plus a boundary integral. The method can be classified into two main categories: vortical impulse integration [14–16] and auxiliary potential-based methods [17, 18]. Complete [18] or incomplete [19, 20] knowledge of vorticity (or velocity) distribution is required. The impulse approaches have seen wide use in PIV data analysis [19, 21] while the auxiliary potential-based approaches have been underutilized, despite their great potential in unsteady flows without containing the time derivatives explicitly. Li & Wu (2018) [22] proposed a vortex force map (VFM) method by adopting Howe's (1995) [18] force formula for the derivation of the vortex force vectors and the construction of the VFM. The VFM is useful to identify the force contributions from each given vortex without knowing the flow field. However, as the derivation was based on inviscid theory, only the pressure force term caused by vorticity in the flow field was considered, while viscous effect was neglected in their work. Moreover, the VFMs in their works cannot reflect the fact that only near-body vorticity is more significant in its effects on the force experienced by the body. In inviscid flow, far-away vorticity (for example, a starting vortex) has a great impact on the force through circulation remaining on the body, sometimes represented by image vorticity within the

body, while for real viscous flows the vorticity at infinity reflects its effect through vorticity in the boundary layer. Thus, it will be preferable, on an intuitive and practical basis, to have a force method only involving near-body vorticity.

To overcome the above drawbacks, this work extends the VFM method of Li & Wu (2018) [22] to more general cases, where the vortex force now consists of four parts: the added mass term; the vortex pressure force caused by free vorticity in the flow field; the viscous pressure force and the skin friction force caused by vorticity in the boundary layer close to the body surface. This work also presents updated vortex pressure force maps based on the vortex pressure force factors derived from viscous governing equations, whose influence from vortices in the flow now vanish as the distance to the body approaches infinity. These maps help us identify the force contribution role of each given vortex more precisely than the ones presented previously. To demonstrate the application of this method, we will apply it to impulsively started flows around a cylinder and a NACA0012 airfoil, with validation against CFD. It is intended that this serves as an analysis of the errors of this method itself before its application to PIV data, thus the accuracy of this approach on small domains and under coarse sampling will also be analyzed using fully converged CFD data.

In Sec. II, the extension of the original VFM approach to more general cases is presented. The way to design vortex pressure force maps and to apply the force approach to calculate total force are also presented.

In Sec. III, vortex pressure force map analyses for a cylinder and a NACA0012 airfoil are demonstrated.

Section IV is devoted to the application of the vortex force approach to unsteady flows around a cylinder and NACA0012 airfoil. The force results given by the extended VFM method are validated against those directly evaluated by CFD. The analysis of different force components is given. The effect of calculation domain and sampling density on the accuracy of the force approach are studied.

Concluding remarks are given in Sec. V.

II. Derivation of the extended VFM method

Consider viscous flows of constant density ρ and viscosity μ around a solid body of volume Ω_B, bounded by a closed surface S_B. In the two-dimensional case, the bounding surface S_B reduces to a closed curve l_B. The control volume is Ω bounded by S_∞ at infinity. The velocity of the flow field is $\overrightarrow{U} = (u, v)$ in the body-fixed frame and $\overrightarrow{U_g} = (u_g, v_g)$ in the ground-fixed frame. The velocity of the body motion is $\overrightarrow{U_B}(t)$. For a special case when the body is moving at a constant velocity, $U_B(t) = -V_\infty$, i.e., in the body-fixed frame, the free stream velocity V_∞ is incident on the body axis at an angle of α as shown in Fig. 1. The vorticity of the flow field is $\overrightarrow{\omega}$. The force acting on the body is $\overrightarrow{F}$, which can be decomposed into a component F_N normal to the axis and an axial component F_A, or a lift component L and a drag component D, as shown in Fig. 1. In the case considered above, the flow in the ground-fixed frame is assumed to be governed by the incompressible momentum equation in the Lamb-Gromyko form

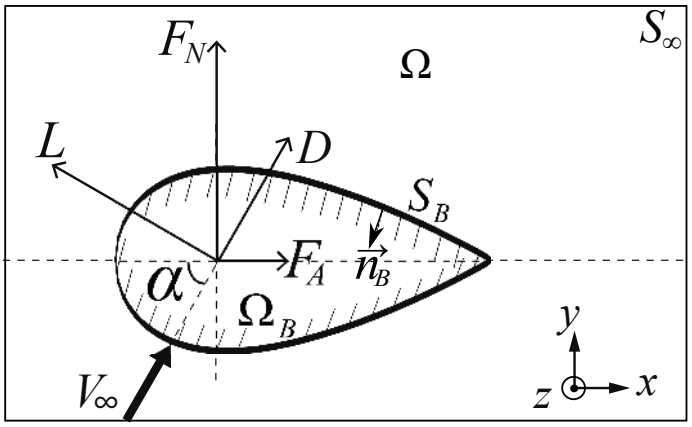

Fig. 1 A rigid body Ω_B, bounded by S_B, in translational outer flows with a control volume Ω bounded by S_∞ at infinity.

$$\nabla\left(P+\frac{1}{2}\rho U_g^2\right)+\rho\vec{\omega}\times\vec{U_g}=-\rho\frac{\partial\vec{U_g}}{\partial t}-\mu\nabla\times\vec{\omega} \tag{1}$$

and the incompressible continuity equation

$$\nabla\cdot\vec{U_g}=0. \tag{2}$$

With $\vec{U_g}=\vec{U}+\vec{U_B}$, we could rewrite the equations (1) and (2) in the body-fixed frame as

$$\nabla\left(P+\frac{1}{2}\rho U^2\right)+\rho\vec{\omega}\times\vec{U}=-\rho\frac{\partial\vec{U}}{\partial t}-\rho\frac{\partial\vec{U_B}}{\partial t}-\mu\nabla\times\vec{\omega} \tag{3}$$

and

$$\nabla\cdot\vec{U}=0. \tag{4}$$

In order to express the force as a function of the vorticity in the flow field and on the body surface, we introduce a set of hypothetical potentials ϕ_k, as suggested by Howe (1995). Each corresponds to the velocity potential for hypothetical fluid motion induced by the translational motion of Ω_B at unit speed in the negative k^{th}-direction. They satisfy the Laplace equation $\nabla^2\phi_k=0$, and vanish at infinity. Note that these hypothetical potentials are not the classic potential flow solution to aerofoils, as no Kutta condition is to be enforced anywhere. According to the definition of the hypothetical potential, we have

$$-\nabla\phi_k\cdot\vec{n_B}=\vec{k}\cdot\vec{n_B}=n_{B,k} \tag{5}$$

on the body surface, where $\vec{n_B}$ is the normal vector pointing inward from the body surface and $\vec{k}$ is the unit vector in k^{th}-direction.

The original VFM method expressed the force as $F_k = \rho \iint_\Omega \nabla\phi_k^* \bullet \overrightarrow{U}\omega_z d\Omega$ [22], where ϕ_k^* is the hypothetical potential defined as the velocity potential induced by unit incident velocity of ideal flow in the k^{th}-direction, $\overrightarrow{U}$ is the local velocity and $\omega_z = \frac{\partial v}{\partial x} - \frac{\partial u}{\partial y}$ is the vorticity defined in two dimensional flow with coordinates (x, y). In this original force formula for the VFM method, the vorticity far from the body does affect the force through the non-zero vortex force factor $\nabla\phi_k^*$ at infinity, and the added mass force and the viscous effect were excluded. Although an additional force term was added to make the force contribution of vortex far from the body to be zero, this physical fact wasn't reflected in the VFMs which were designed according to the vortex force factors $\nabla\phi_k^*$. To overcome the aforementioned shortcomings, an extended VFM method will be derived in this section.

A. Normal and axial force formula for the extended VFM method

Considering a translational moving of the body with a velocity $\overrightarrow{U_B}(t)$, through a rigorous derivation (see Appendix A) of the force formula directly from the viscous governing equations (1) and (2), with the introduction of the hypothetical potentials described in equation (5), we get the expression for the body force in two dimensions,

$$\begin{cases} F_k = F_k^{(add)} + F_k^{(vp)} + F_k^{(vis-p)} + F_k^{(vis-f)} \\ F_k^{(add)} = \oint_{l_B} \phi_k \frac{d\overrightarrow{U_B}}{dt} \bullet \overrightarrow{n}\, dl \\ F_k^{(vp)} = \rho \iint_\Omega \overrightarrow{\Lambda}_k \bullet \overrightarrow{U}\omega_z d\Omega \\ \left.\begin{array}{l} F_k^{(vis-p)} = \mu \oint_{l_B} \omega_z d\phi_k \\ F_k^{(vis-f)} = \mu \oint_{l_B} \omega_z \overrightarrow{k} \bullet \overrightarrow{dl} \end{array}\right\} F_k^{(correction)} \end{cases} \tag{6}$$

Note that this method can be easily extended for complex body motions (e.g.pitching airfoils) by rewriting equations (1) and (2) in the corresponding non-inertial body-fixed frame, and defining the velocity at any point of the body surface as $\overrightarrow{U_B}(t) + \overrightarrow{\omega_B}(t) \times (\overrightarrow{x} - \overrightarrow{x_0})$, where $\overrightarrow{\omega_B}(t)$ is the angular velocity of the body.

The integral in vortex pressure force term of Equation (6) is defined within the whole fluid region Ω, and the viscous pressure and skin-friction terms along the body surface l_B. The vortex pressure force factor is expressed as

$$\overrightarrow{\Lambda}_k = \left(\frac{\partial\phi_k}{\partial y}, -\frac{\partial\phi_k}{\partial x}\right). \tag{7}$$

Here ϕ_k is the hypothetical potential defined in the beginning of this section. Equation (6) can be used to calculate the normal force F_N and the axial force F_A by choosing the k^{th}-direction as the normal (N) and axial (A) direction, and the corresponding vortex pressure force factors $\overrightarrow{\Lambda}_N$ and $\overrightarrow{\Lambda}_A$ are given in expression (7). The potentials ϕ_N and ϕ_A are

different from the definition in Li & Wu 2018 [22], which can be obtained by solving the new Laplace models below.

$$\begin{cases} \frac{\partial^2 \phi_N}{\partial x^2} + \frac{\partial^2 \phi_N}{\partial y^2} = 0 \\ \frac{\partial \phi_N}{\partial y} = 1, \frac{\partial \phi_N}{\partial x} = 0 \quad (x, y) \to l_B \\ \frac{\partial \phi_N}{\partial y} = 0, \frac{\partial \phi_N}{\partial x} = 0 \quad (x, y) \to \infty \end{cases} \tag{8}$$

$$\begin{cases} \frac{\partial^2 \phi_A}{\partial x^2} + \frac{\partial^2 \phi_A}{\partial y^2} = 0 \\ \frac{\partial \phi_A}{\partial y} = 0, \frac{\partial \phi_A}{\partial x} = 1 \quad (x, y) \to l_B \\ \frac{\partial \phi_A}{\partial y} = 0, \frac{\partial \phi_A}{\partial x} = 0 \quad (x, y) \to \infty \end{cases} \tag{9}$$

Note that, the second term $F_k^{(vp)}$ in expression (6) is all that was considered in the previous paper. But here $\nabla \phi_k = 0$ at infinity, thus the requirement that only near-body vortices have important effects on the vortex-induced body-force is automatically satisfied. This is in accordance with the fact that only near-body vortices are more likely to cause pressure variation while vortices far away from the body have negligible effects on force.

The inclusion of added mass force $F_k^{(add)}$ here allows us to deal with flows concerning more general body motions in addition to impulsively started flows. The inclusion of viscous terms $F_k^{(vis-p)}$ and $F_k^{(vis-f)}$ faciliates its capability for low Reynolds number viscous flows. Through this force decomposition, we find that viscosity contributes to not only the well known skin friction force $F_k^{(vis-f)}$, but also the pressure force $F_k^{(vis-p)}$, through the vorticity diffusion on the body surface. Or we can think of it as a correction from displacement effect of the body surface caused by viscous boundary layer. More details will be discussed in later sections.

Another point to note is that unsteady effects are included in the force formula despite t not appearing explicitly, as $\overrightarrow{\omega}$ and $\overrightarrow{U}$ are both time-dependent, which means that the temporal resolution of flow field data does not affect the accuracy of our method.

B. Lift and drag formulas for the extended VFM method

For a specific angle-of-attack (AoA) of α, the lift and drag can be proved to have exactly the same form as expression (6), with the k^{th}-direction replaced by the lift (L) and the drag (D) direction, respectively. The vortex force factors for lift and drag can be calculated by

$$\begin{cases} \overrightarrow{\Lambda}_L = \overrightarrow{\Lambda}_N \cos\alpha - \overrightarrow{\Lambda}_A \sin\alpha \\ \overrightarrow{\Lambda}_D = \overrightarrow{\Lambda}_N \sin\alpha + \overrightarrow{\Lambda}_A \cos\alpha \end{cases}, \tag{10}$$

and the hypothetical potential can be obtained in a similar way.

$$\begin{cases} \phi_L = \phi_N \cos\alpha - \phi_A \sin\alpha \\ \phi_D = \phi_N \sin\alpha + \phi_A \cos\alpha \end{cases} \tag{11}$$

C. The vortex pressure force maps and calculation of total force

Expression (6) with k^{th}-direction chosen as the lift ((L)) and drag ((D)) direction, gives the lift and drag as a function of the vorticity field, in which the free vorticity in the flow field contributes to the pressure force and the vorticity in the boundary layer close to the body surface contributes to both pressure force and skin-friction force. As will be discussed later, the dominant force component is vortex pressure force, and the vortex pressure force contains the vortex pressure force factors defined in (10), similar to the vortex force factors in Li & Wu (2018) [22], which are a function of position but independent of the flow field and only dependent on the body shape and the angle of attack. Thus the vortex pressure force maps can be made in a similar way to help analyze the behaviour of fluid forces with relation to the vortex pattern in the flow field, and to identify favorable direction and critical regions for positive and negative force production by a given vortex. The force formula (6) here can also be used to obtain total force if the properties of vortices (velocity and circulation) in the flow field and on the body surface are obtained by some analytical, numerical or experimental methods.

a) *vortex pressure force map analysis*

Similar to the previous work of Li & Wu (2018)[22], here the vortex force map in the two-dimensional plane (x, y) contains force lines that are locally parallel to the vortex force vector ($\overrightarrow{\Lambda}_N$ for normal force and $\overrightarrow{\Lambda}_A$ for axial force with $\overrightarrow{\Lambda}_N$ and $\overrightarrow{\Lambda}_A$ given by (7) with k^{th}-direction chosen as the normal (N) and axial (A) direction, $\overrightarrow{\Lambda}_L$ for lift force and $\overrightarrow{\Lambda}_D$ for drag force with $\overrightarrow{\Lambda}_L, \overrightarrow{\Lambda}_D$ given by (10)). Vortex force lines, independent of specific flow conditions, can then be obtained through a streamline procedure, with the velocity replaced by the vortex force factors. As a quick reminder, the auxiliary potentials defined in this work are different from those in in Li & Wu (2018) [22], which leads to the difference in VFMs.

Any individual vortex has a force contribution, which can be easily identified according to its circulation (sign and magnitude), position and direction (the angle between the vortex force line and streamline at the position of the vortex). Thus a vortex force map analysis can be used to identify direction and critical regions for positive and negative force production of a given vortex as in Li & Wu (2018) [22].

b) *Calculation of total force*

The vortex force factors can be precomputed for a rigid body, the force can then be directly obtained from the vortex force formulas once $\overrightarrow{U}$ and ω_z are computed or measured. This can be done as follows.

Given the geometry of the airfoil, we solve (8)-(9) to get ϕ_N and ϕ_A, then put these ϕ_N and ϕ_A into (7) to get the

vortex force factors $\overrightarrow{\Lambda}_N$ and $\overrightarrow{\Lambda}_A$. These factors only depend on the geometry (shape of the body) and are independent of other flow conditions including angle of attack and Reynolds number. The flow vorticity ω_z and velocity $\overrightarrow{U}$ may be obtained by conventional methods (discrete vortex simulation, computational fluid dynamics simulation, experimental measurement).

The force factors $\overrightarrow{\Lambda}_L$ and $\overrightarrow{\Lambda}_L$ can be obtained by substituting $\overrightarrow{\Lambda}_N$ and $\overrightarrow{\Lambda}_A$ into (10), and the hypothetical potentials ϕ_L and ϕ_D can be obtained by substituting ϕ_N and ϕ_A into (11). Then the three force terms of expression (6) with the k^{th}-direction replaced by the lift (L) and the drag (D) direction, can be used to obtain the vortex pressure force, the viscous pressure force, and the skin-friction force, respectively.

For cylinders or simple airfoils (e.g., flat plate and Joukowsky airfoil), equations (8) and (9) have analytical solutions. For more general shapes, ϕ_N and ϕ_A can easily be computed numerically. Their use will be demonstrated in the next section.

III. vortex pressure force map analysis for cylinder and general airfoils

In this section, a cylinder and a NACA0012 airfoil are used to demonstrate the construction of vortex pressure force maps and how it is used to identify the force contribution role of each given vortex according to its position, strength and local velocity. Here we only consider lift and drag force maps, which depend on angle of attack.

A. vortex pressure lift/drag maps for a cylinder

For a circular cylinder of radius a, the analytical solutions ϕ_N and ϕ_A for Laplace equations (8) and (9) can be easily constructed by superposition, the results are

$$\phi_N = \frac{a^2 y}{x^2+y^2}, \phi_A = \frac{a^2 x}{x^2+y^2}. \tag{12}$$

Inserting (12) for into (7) gives the vortex pressure force factors for lift

$$\overrightarrow{\Lambda_N} = \left(\frac{\left(x^2-y^2\right) a^2}{\left(x^2+y^2\right)^2}, \frac{2xya^2}{\left(x^2+y^2\right)^2} \right) \tag{13}$$

and drag

$$\overrightarrow{\Lambda_A} = \left(-\frac{2xya^2}{\left(x^2+y^2\right)^2}, \frac{\left(x^2-y^2\right) a^2}{\left(x^2+y^2\right)^2} \right). \tag{14}$$

As mentioned above, for a cylinder with $\alpha = 0^o$, we have

$$\phi_L = \phi_N, \phi_D = \phi_A, \overrightarrow{\Lambda_L} = \overrightarrow{\Lambda_N}, \overrightarrow{\Lambda_D} = \overrightarrow{\Lambda_A}. \tag{15}$$

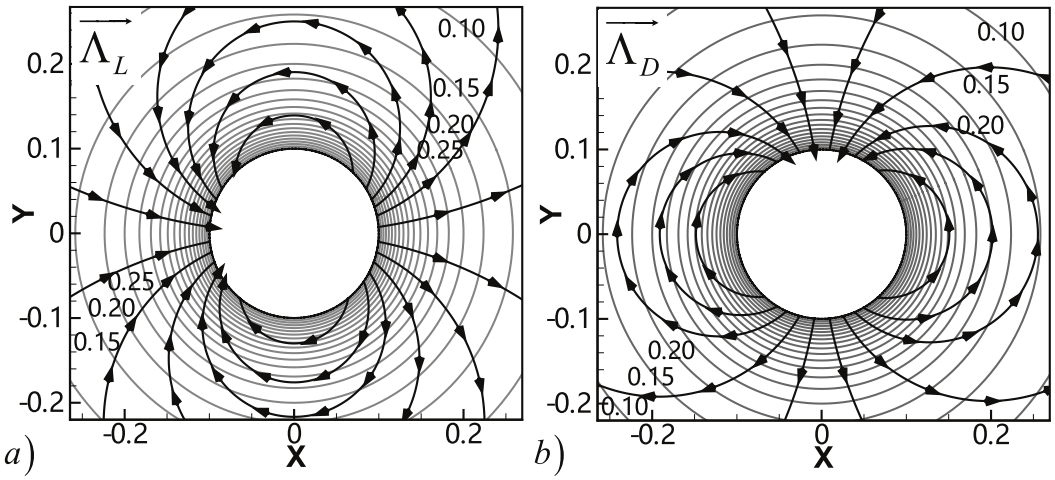

Fig. 2 vortex pressure froce maps for lift (a) and for drag (b) of a cylinder.

With the vortex pressure force factor given by (15), we can draw the vortex pressure lift/drag maps as shown in figure 2(a-b) where the lines with arrows are vortex pressure force lines locally parallel to the vector $\overrightarrow{\Lambda_L}$ and $\overrightarrow{\Lambda_D}$, and the lines without arrows are contours of magnitude of $\overrightarrow{\Lambda_L}$ and $\overrightarrow{\Lambda_D}$.

Figure 2(a) is the vortex pressure lift map for a cylinder with $a = 0.1$. As in Li & Wu (2018) [22], each arrowed force line defines the most favourable direction for a counterclockwise vortex (having positive strength) to give a positive lift or most unfavourable direction for a clockwise vortex (having negative strength) to give a negative lift. We can see that the vortex pressure lift map is symmetrical about the $y = 0$ axis. This explains that a pair of counter rotating vortices moving symmetrically downstream of a cylinder contribute zero lift.

Figure 2(b) is the vortex pressure drag map for a cylinder with $a = 0.1$. A counterclockwise vortex provides positive drag (thrust), while a clockwise vortex provides negative drag, when it moves along or at an acute angle to the vortex pressure drag lines. The sign of the drag changes if the moving direction is reversed. We can see that the vortex pressure drag map is symmetrical about $x = 0$ axis, and anti-symmetrical about the $y = 0$ axis, which means that a pair of counter rotating vortices moving symmetrically downstream of a cylinder contribute twice the drag caused by one single vortex.

B. vortex pressure lift/drag maps for a NACA0012 airfoil

For the NACA0012 airfoil, the Laplace equations (8) and (9) are solved numerically to give ϕ_N and ϕ_A. We have used here the heat transfer option in the commercial code CFX as a solver of the present Laplace equation, which procedure has been validated in Li & Wu (2018) [22]. The grid used here are in accordance with that used in obtaining the flow field by computational fluid dynamics, which will be demonstrated in the next section. The vortex pressure force factors for normal ($\overrightarrow{\Lambda_N}$) and for axial force ($\overrightarrow{\Lambda_A}$) are then computed by (7). With angle of attack given, put these $\overrightarrow{\Lambda_N}$ and $\overrightarrow{\Lambda_A}$ into (10), we have the vortex pressure lift and drag factors $\overrightarrow{\Lambda_L}$ and $\overrightarrow{\Lambda_D}$.

Figure 3 shows the vortex pressure force maps for both lift and drag of the NACA0012 airfoil at angles of attack 20^o,

45^o and 60^o. They are plotted according to the method described in section 2.3. In Figure 3, the lines with arrows are vortex pressure force lines locally parallel to the vector $\overrightarrow{\Lambda_L}$ and $\overrightarrow{\Lambda_D}$, and the lines without arrows are contours of magnitude of $\overrightarrow{\Lambda_L}$ and $\overrightarrow{\Lambda_D}$.

We mention that the appearance of the vortex pressure force maps here is quite different from that in Li & Wu (2018) [22], although constructed in a similar way. This is because of the difference in the definition of the vortex force factors. In viscous flows, the circulation about the body associated with the starting vortex at infinity is not represented as an image vortex inside the body, but as the vorticity in the boundary layer. Thus the fact that vorticity far-away from the body has negligible effect on force should be reflected in the VFMs. As we can see from Figures 2 and 3, the magnitude of vortex pressure force factors $\left|\overrightarrow{\Lambda_L}\right|$ and $\left|\overrightarrow{\Lambda_D}\right|$ decrease with the distance from the body surface and vanish at infinity. Thus, the present vortex force maps are able to describe the force contribution role of vorticity in the flow field more precisely than the previous ones.

Figure 3(a,c,e) are for lift. An leading edge vortex (LEV) (trailing edge vortex (TEV)) provides positive (negative) lift if it moves so as to have a component of motion opposed to the vortex pressure lift lines, and vice versa.

Figure 3(b,d,f) are for drag. An LEV (TEV) provides drag (thrust) if it moves so as to have a component of motion opposed to the vortex pressure lift lines, and vice versa.

In both maps we can see that, the force lines diverge from the trailing edge and gather together at the leading edge, and the angle of attack seems to have a rotating and deforming effect on force lines.

IV. Lift and drag prediction for viscous flows around an impulsively started cylinder and NACA0012 airfoil using VFM

In this section, the extended VFM method is applied to an impulsively started flow around a cylinder and the NACA0012 airfoil. Here, the total force will be given by (6) with the k^{th}-direction chosen as the lift (L) and the drag (D) direction, and with the velocity and vorticity field provided by computational fluid dynamics. The force formula (6), used without the first term (added mass) yields an accurate force prediction for the impulsively started case considered here, as $\left.\frac{\partial \vec{U}}{\partial t}\right|_{S_B} = \infty$ at the initial instant, and $\left.\frac{\partial \vec{U}}{\partial t}\right|_{S_B} = 0$ at any other time. Here all the flow field is assumed to be laminar. The lift and drag predictions from VFM will be compared with those obtained from integrating the body surface pressure and skin-friction given by CFD code. The contribution of different force components, contributed from free vorticity in the flow field or from the body surface vorticity, will be discussed. The purpose of this exercise is to not only just study the validity of the extended VFM method, but also to explore its potential application in load estimation for experiments such as Particle Image Velocimetry (PIV). Thus, the influence of the size of a truncated computational domain and the resolution on the accuracy of this approach will also be investigated.

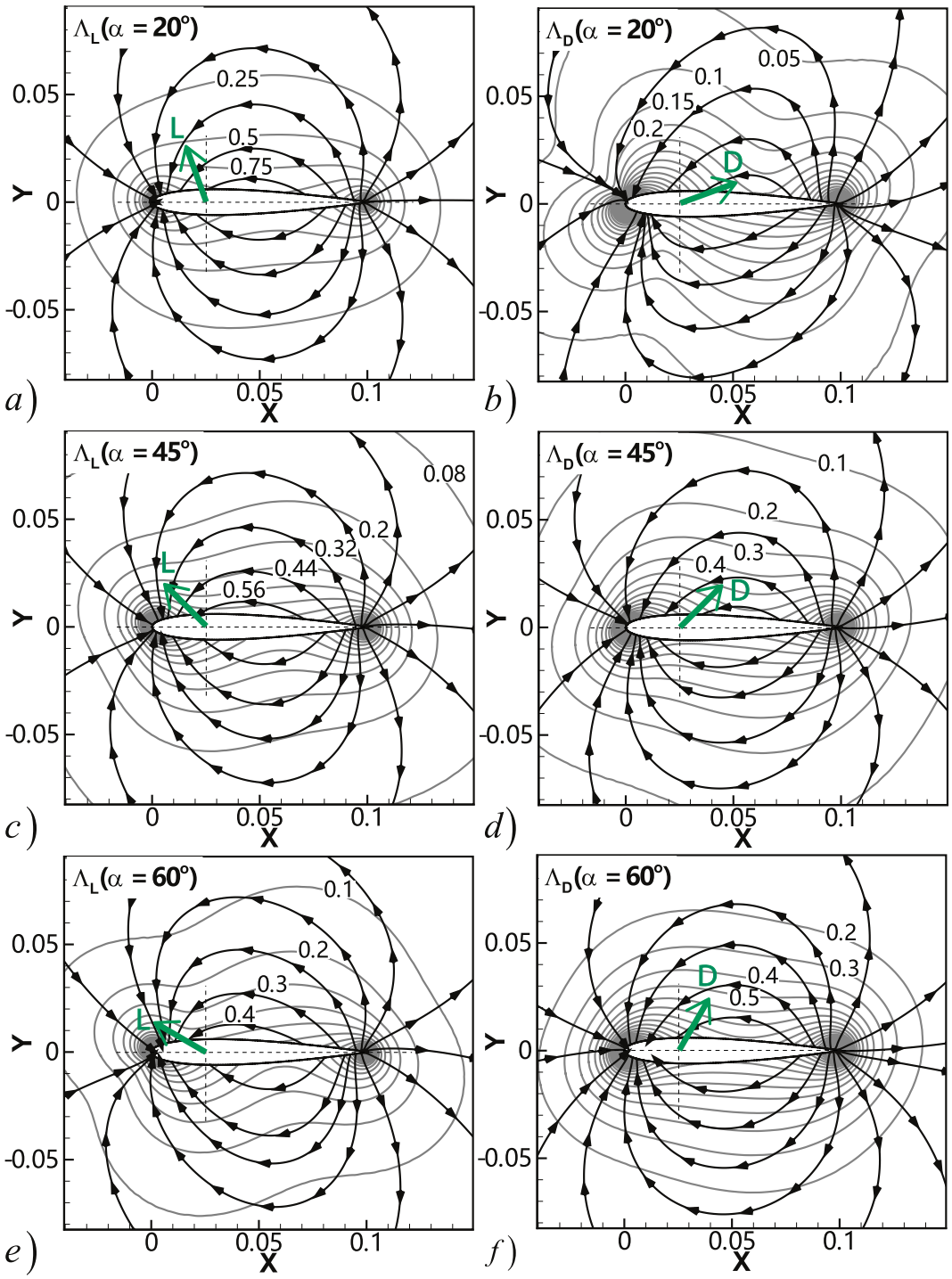

Fig. 3 vortex pressure force maps for lift and for drag of NACA0012 airfoil: (a),(c),(e) are for lift at $\alpha = 20^o$, 45^o and 60^o; (b),(d),(e) are for drag at $\alpha = 20^o$, 45^o and 60^o, respectively.

A. Force approach and CFD method

As discussed in section 2.3, the vortex force approach (6) can be used to calculate the total force acting on the body, with the vortex force factors precomputed by analytical or numerical methods, and the velocity and vorticity field given by simulations such as vortex panel method, computational fluid dynamics simulation, or from experimental measurement. Here the results of the force prediction will be compared to the lift and drag obtained from the integration of the body surface pressure and skin friction in CFD. We present the force predictions in the form of non-dimensional coefficients. The lift coefficient and drag coefficient are defined as

$$C_L = \frac{L}{\frac{1}{2}\rho V_\infty^2 \ell_B}, C_D = \frac{D}{\frac{1}{2}\rho V_\infty^2 \ell_B} \tag{16}$$

where ℓ_B is the characteristic length of the body, chosen to be the diameter ($\ell_B = 2a$) for a cylinder and the chord length ($\ell_B = c_A$) for a general airfoil. The non-dimensional time is written as $\tau = tV_\infty/\ell_B$.

In the CFD simulation used in this work, the Navier–Stokes equations in unsteady laminar flow are solved numerically using the same method as used by Li & Wu (2018) [22]. We have used the commercial code Fluent with the options of a second-order upwind SIMPLE (semi-implicit method for pressure-linked equations) pressure–velocity coupling method. The computational domain is 36 diameters in the horizontal direction and 21 diameters in the vertical direction for a cylinder, and 31 chord lengths in the horizontal direction and 20 chord lengths in the vertical direction for a NACA0012 airfoil. Different mesh sizes are chosen for different Reynolds numbers. For a cylinder, four Reynolds numbers 200, 500, 1000 and $1e6$ are considered. Correspondingly, meshes with 55375, 64190, 80197 and 268814 grid points in total, and with 314, 419, 628 and 2673 grids on the body surface are used. For a NACA0012 airfoil, three different meshes are used for 6 different Reynolds numbers. A mesh with 115072 grid points in total and with 102 grids on the surface is used in the CFD simulation of $Re = 50, 100$ and 200. A mesh with 127494 grid points in total and with 184 grids on the surface is used for $Re = 500$ and 1000. A mesh with 174910 grid points in total and with 550 grids on the surface is used for $Re = 1e6$. The mesh size normal to the wall and in the boundary layer is refined to a minimum of 30 layers. Grid-converged check has been carried out here. The flow is impulsively started at a constant from an initially uniform flow. The flow is unsteady and the present VFM method is capable of describing the vortex force at any instant, even when some early shed vortices have moved very far-away from the body.

As a validation for the CFD method used here, numerical results for time-averaged lift and drag for NACA 0012 airfoils at different Reynolds numbers are compared with those from experiments in Fig. 4. We can see that the CFD results at $Re = 1e4$ compare well with experimental data both from Zhou et al. (2011) [23] for $Re = 1.05e4$ and from Ohtake et al. (2007) [24] for $Re = 1.0e4$. The CFD results at $Re = 1e6$ also agree well with experimental data from Critzos et al. (1955) [25] for $Re = 1.8e6$.

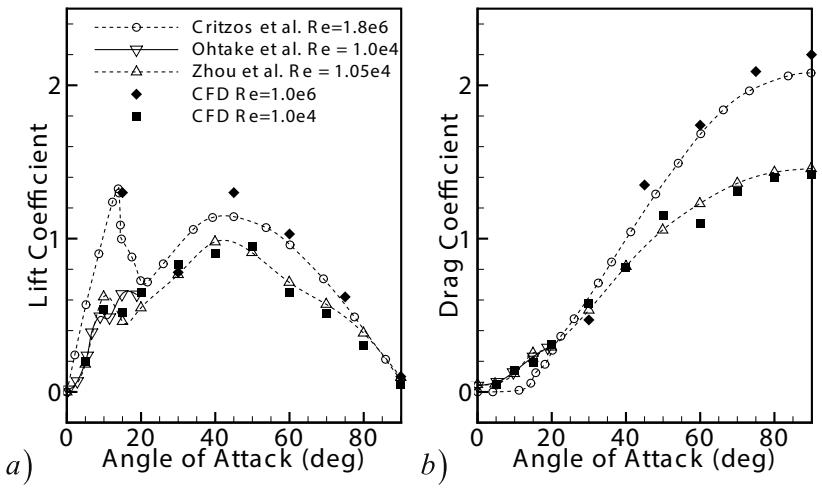

Fig. 4 Comparison of time-averaged lift (a) and drag (b) for a NACA 0012 airfoil at angle of attacks from 0^o to 90^o obtained from experiments and numerical simulations.

B. Vortex lift and drag for viscous flows around a cylinder

First, we apply the present VFM method to the cylinder flow at different Reynolds numbers 200, 500, and $1e6$. Figure 5 shows good agreement between VFM theory and CFD force results for both lift and drag coefficients. The viscous correction terms for lift and drag are also shown in Fig. 5. It can be seen that the viscous correction for lift oscillates about a zero average value and the oscillation amplitude decreases as the Reynolds number increases. The viscous correction for drag decreases from an initial value to a relative stable value, as the vorticity on the body surface decreases from an initial transient. For $Re = 1e6$, the viscous correction terms for both lift and drag are negligible.

The vortex flow pattern (shown as streamlines in Fig. 5(d)), together with vortex pressure force map (shown in section 3.1), can reveal the physical mechanisms behind the variation of lift and drag. We can see that the lift oscillates around 0 and the oscillation amplitude increase with time and reaches a stable value due to the growth and alternative shedding of a pair of vortices. The initial rise of pressure drag coefficient is due to the rapid increase of $|\omega_z|$ on the lee side and its movement along the drag increasing direction. Then the drag drops as the concentrated region of vorticity on the lee side disperses far away from the body, where the magnitude of vortex pressure drag factor is low. After a slight rise, it reaches a periodic oscillation around an average value due to the alternate shedding of the vorticity.

Figure 6(a-b) show the different components of force coefficients for cylinder from the VFM method at $Re = 200$, as well as the total force coefficients from CFD. Figure 6(a) is for lift and Fig. 6(b) is for drag. We can see from these figures that the vortex pressure force is the dominant force, which is responsible for the force oscillation behavior. Moreover, viscous pressure force and skin friction force coincide for the cylinder flow case considered here. Actually this coincidence is not unexpected. If we substitute equations (12) and (15) into equation (6), we could get the result for a circular cylinder that

$$L^{(vis-p)} = L^{(vis-f)}, D^{(vis-p)} = D^{(vis-f)}. \tag{17}$$

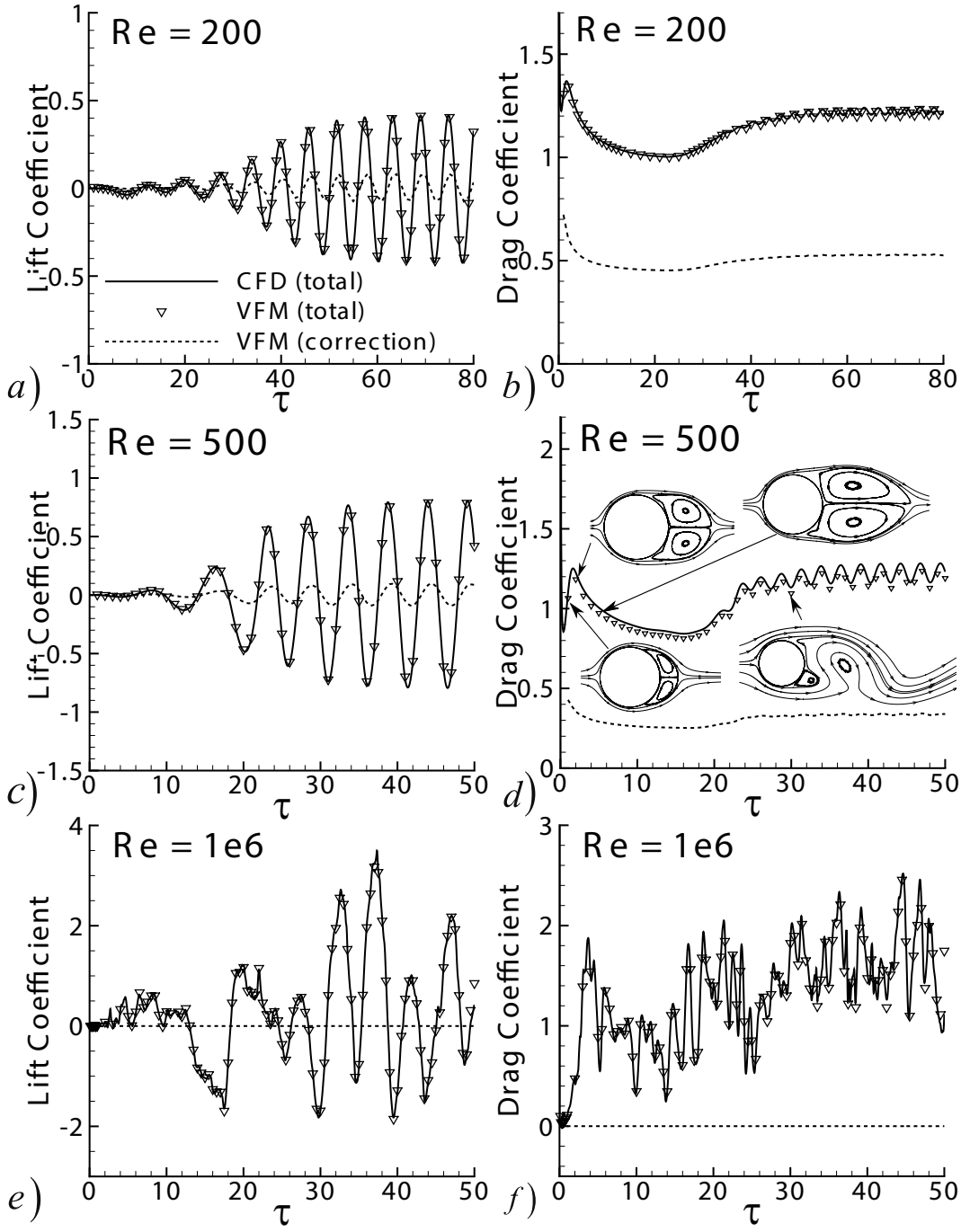

Fig. 5 Comparison between theory and CFD for time-dependent lift coefficients for cylinder at $Re = 200, 500,$ **and** $1e6$**.**

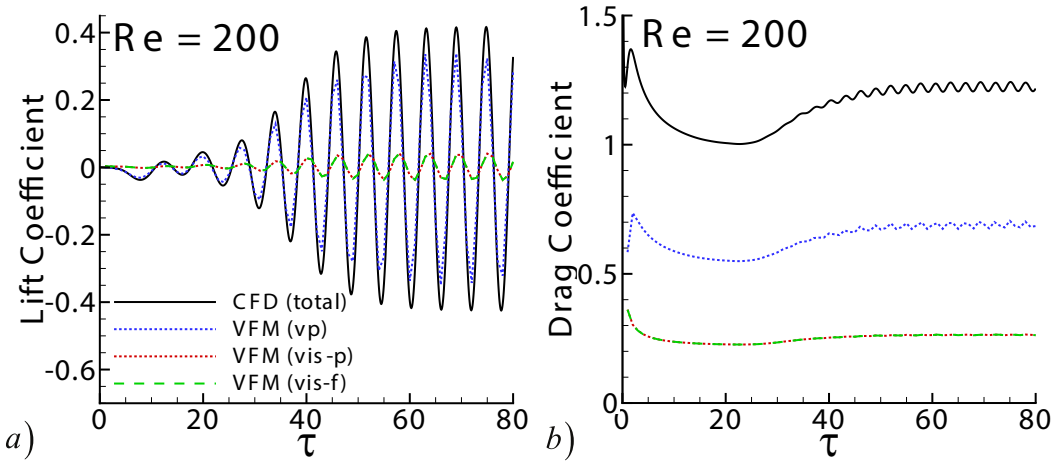

Fig. 6 Different components of lift and drag coefficients for cylinder at $Re = 200$**.**

C. Vortex lift and drag for viscous flows around a NACA0012 airfoil

Applying the extended VFM method to NACA0012 airfoil, we also find good comparison between theory and CFD for $\alpha = 60^o$ at different Reynolds numbers (Re = 50, 500, and $1e6$), as shown in Fig. 7 (a,c,e) for lift and in Fig. 7 (b,d,f) for drag. The small discrepancy between the CFD and VFM methods comes from the numerical errors both in solving Navier-Stokes equations and in evaluating the integrals in equation (6).

Figure 8(a-b) show the comparisons of total force coefficient between theory and CFD results at Re = 50, as well as the three force components. Figure 8(a) is for lift and Fig. 8(b) is for drag. We can see that when the Reynolds number is low (Re = 50) the vortex pressure force and viscous pressure force are the dominant force and have the same order of magnitude, while the skin friction force is much lower than either. The overall vortex pressure force and the total force are similar, which means that the force oscillation behavior is contributed primarily from the vortex pressure force. The total force curve against non-dimensional time can be divided into four repeatable stages, and the physical mechanism can be explained by the evaluation of vortex flow patterns in the same way as Li & Wu (2016) [10].

D. Influence of computational domain and sampling density

In order to explore the applicability of the proposed extended VFM method for load estimation in experiments such as PIV, the influence of the size of the computational domain and the sampling density (i.e. resolution) on the accuracy of this approach will be studied in this subsection.

1. The force contribution of the distributed vorticity in the flow field

By normalizing the vortex pressure force term in equation (6), we have the total vortex pressure lift and drag coefficients as well as their spatial distribution as follows

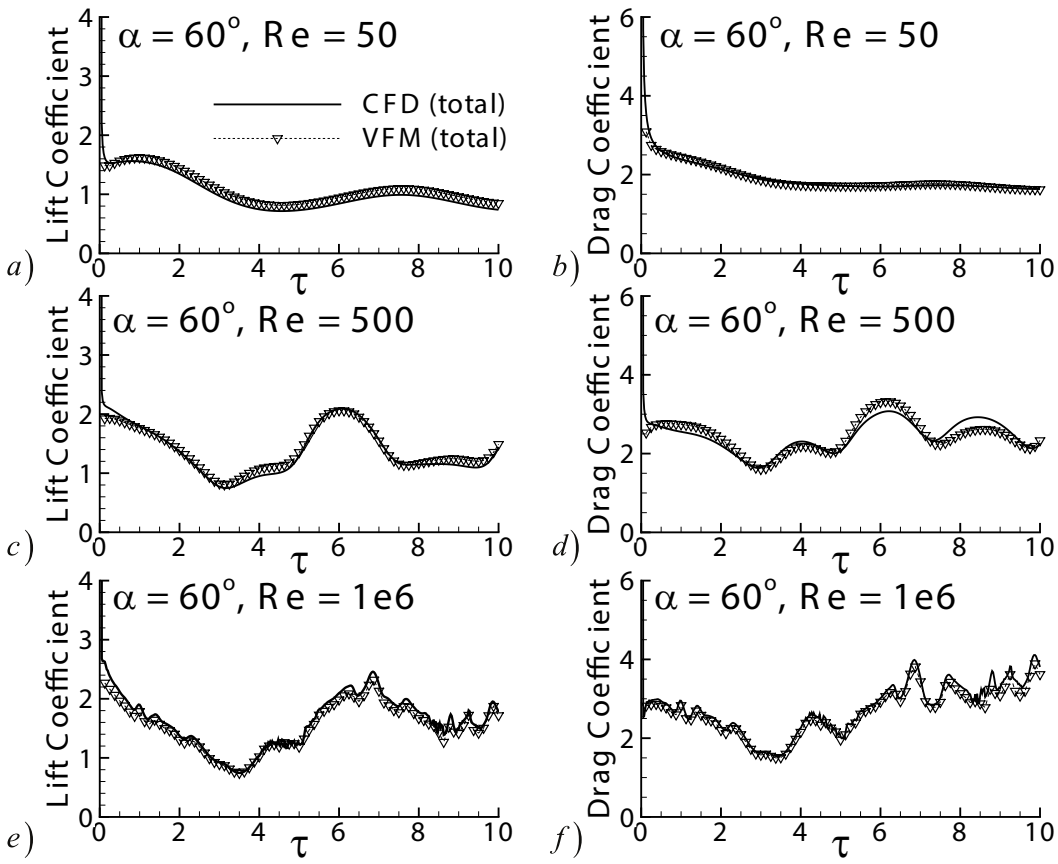

Fig. 7 Comparison between theory and CFD for time-dependent lift coefficients for NACA0012 airfoil at $Re = 50, 100, 200, 500, 1000$ **and** $1e6$**.**

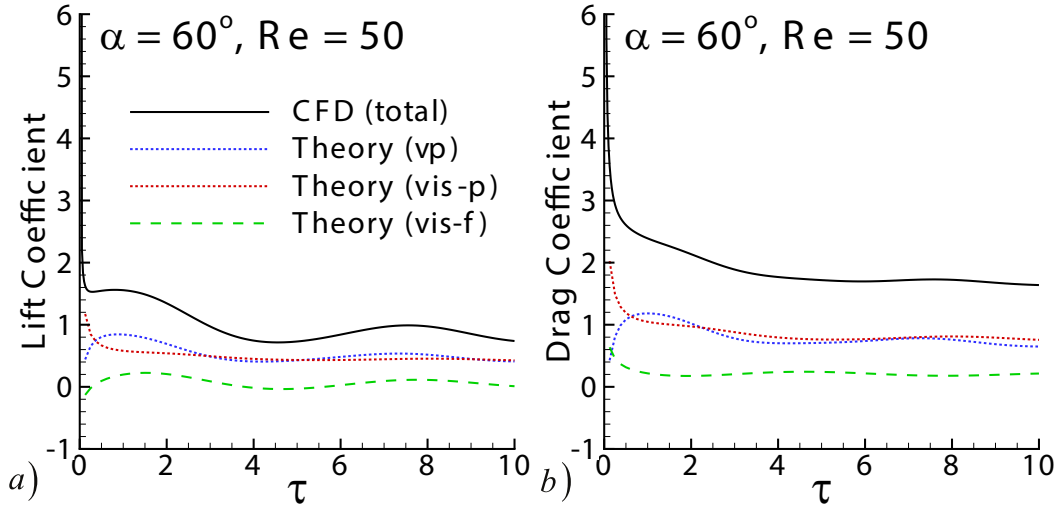

Fig. 8 Different components of lift and drag coefficients for NACA0012 airfoil at $Re = 50$**.**

$$\begin{cases} C_L^{(vp)} = \iint_\Omega \frac{dC_L^{(vp)}}{d\Omega} d\Omega, \ \frac{dC_L^{(vp)}}{d\Omega} = \frac{2\vec{\Lambda}_L \bullet \vec{U}\omega_z}{V_\infty^2 \ell_B} \\ C_D^{(vp)} = \iint_\Omega \frac{dC_D^{(vp)}}{d\Omega} d\Omega, \ \frac{dC_D^{(vp)}}{d\Omega} = \frac{2\vec{\Lambda}_D \bullet \vec{U}\omega_z}{V_\infty^2 \ell_B} \end{cases} .$$

The lift and drag distribution ($dC_L^{(vp)}/d\Omega$ and $dC_D^{(vp)}/d\Omega$) due to vortices in each grid cell in the cylinder case at $Re = 1000$ and at a typical instant ($\tau = 40$) are shown in Figures 9(a) and (b), and the vorticity distribution is shown in Fig. 9 (c). The lift and drag distribution ($dC_L^{(vp)}/d\Omega$ and $dC_D^{(vp)}/d\Omega$) for the NACA0012 airfoil at $\alpha = 60^o$ and for $Re = 1e6$ at a typical instant ($\tau = 6$) are shown in Figures 10 (a) and (b), and the vorticity distribution is shown in Figure 10 (c).

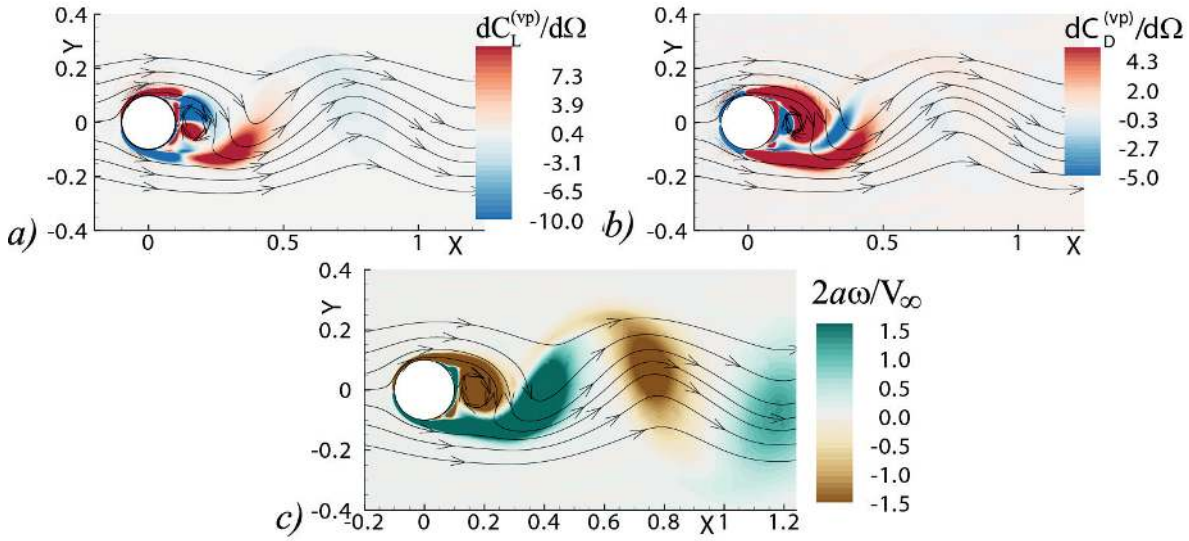

Fig. 9 Vortex pressure lift (a) and drag (b), as well as the vorticity (c) distribution around a cylinder at instant $\tau = 40$ for $Re = 1000$.

In figures 9 and 10, a red color indicates a positive force contribution, while a blue color indicates a negative one. A green color indicates a positive vorticity, while a yellow color indicates a negative one. The theoretical force coefficients are obtained by summing the force coefficients of vortices inside all grid cells in the calculation domain. We can see that each concentrated vortex contain a positive force contribution part and a negative force contribution part. It is shown that the near-body vortices contribute more to the body force than the far away vortices, which is consistent with the Biot-Savart law and allows us to calculate the body forces by using the vorticity in a small area containing the body.

2. Force calculation from truncated domain and coarse mesh

Here different domains $A1$, $A2$, and $A3$ are chosen for the integration of the body force, where $A1$ represents the whole simulation domain for CFD; $A2$ is an area with a length of $11d$ and a width of $10d$ for a cylinder and with a length of $6c_A$ and a width of $6c_A$ for a NACA0012 airfoil; $A3$ represents a truncated domain with a length of $5d$ and a width of

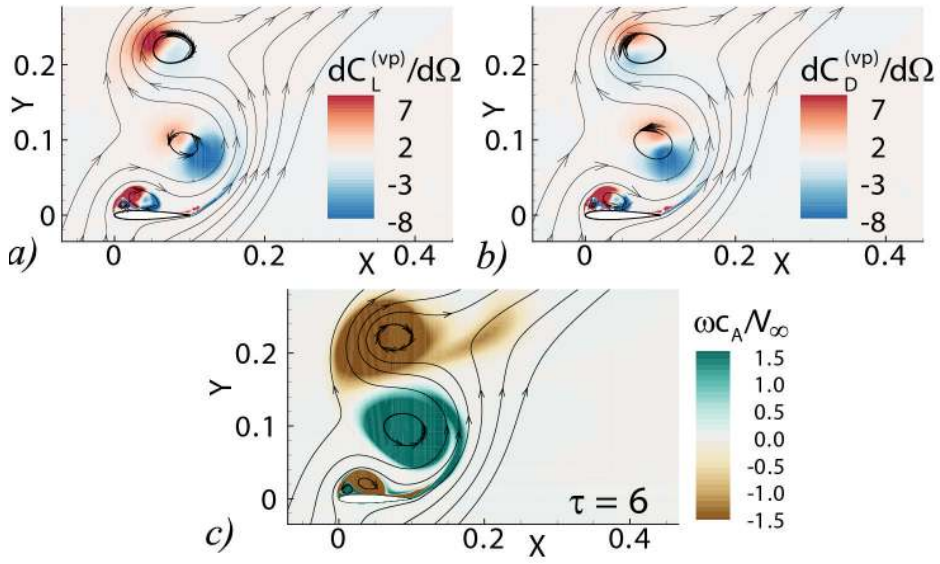

Fig. 10 Vortex pressure lift (a) and drag (b), as well as the vorticity (c) distribution around a cylinder at instant $\tau = 6$ for $Re = 1e6$.

$5d$ for a cylinder and with a length of $3c_A$ and a width of $3c_A$ for a NACA0012 airfoil. Note that the viscous pressure force and friction force are dependent on the vorticity at the body surface, which have no relationship with the domain we choose. For the smallest domain $A3$, the converged flow data (velocity (u, v)) from CFD results computed on one resolved grid are interpolated to two different coarse meshes, The first one (labelled as 'Coarse1' in Figures 11 and 12)) has 230×230 approximately uniform structural grids in total, and the second one (labelled as 'Coarse2' in Figures 11 and 12) has 116×116 mesh grids. Note that the full resolution is roughly 628×115 mesh grids for the cylinder case and 550×245 mesh grids for the NACA0012 case. Note that most of the full grid cells are distributed in the boundary layer, while the coarse meshes have nearly uniform distribution which is similar to typical PIV-measurement data.

Figure 11 shows the comparison of lift and drag of a cylinder at $Re = 1000$ calculated by CFD and by VFM method on different domains and different coarse-sampled mesh. Figure 12 is the results for a NACA0012 airfoil at $Re = 1e6$. We can see from these figures that there are no perceptible differences between forces calculated on domain A_1 and A_2, and they all agrees well with the CFD results. The forces obtained on domain A_3 are slightly different from those on A_1 and A_2, but they also agree well with the CFD results. Thus, if the vorticity field (or velocity field) in a small domain A_3 around the body is known, we are able to predict the force experienced on a body accurately using the VFM method. It can be also seen from Figures 11 and 12 that in general, the coarser the mesh is, the larger the error are, but the errors in these test cases are all in acceptable ranges. Table 1 shows the Relative Root Mean Square Error of Prediction (RRMSEP) defined as follows

$$RRMSEP = \frac{\sqrt{\sum_{i=1}^{N}(y_i - y_{CFD,i})^2/N}}{\sqrt{\sum_{i=1}^{N} y_{CFD,i}^2/N}} \times 100\%,$$

where y_i refers to the C_L or C_D predicted by VFM method at sampling point i, while $y_{CFD,i}$ is the C_L or C_D calculated by CFD at the same sampling point. From the data in Table 1, we could recommend that flow field data with a domain size larger than $3\ell_B \times 3\ell_B$ and a resolution in the order of 100 in each direction would give reasonable results for estimated force (with an error < 20%), which could be easily achieved in PIV-measurements.

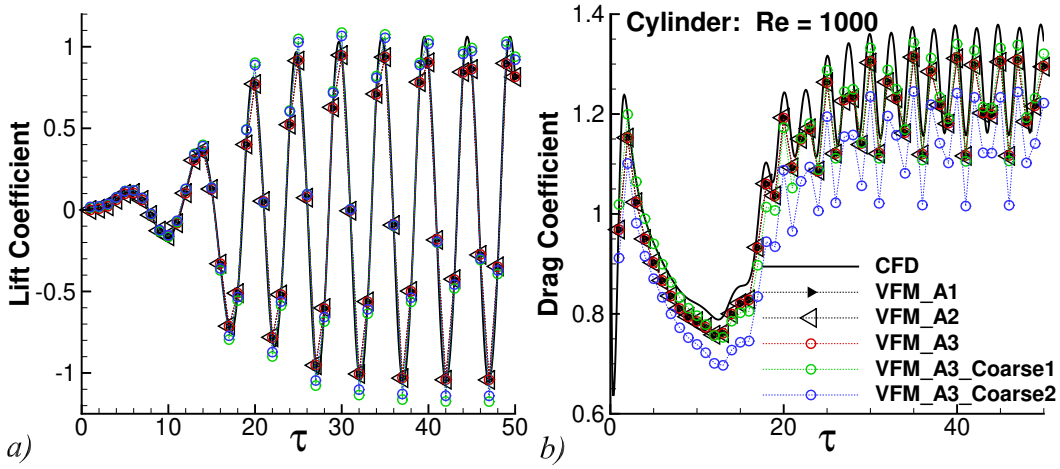

Fig. 11 Comparison of force coefficients from converged CFD results and from VFM method with different domain size and coarse sampling for cylinder at $Re = 1000$.

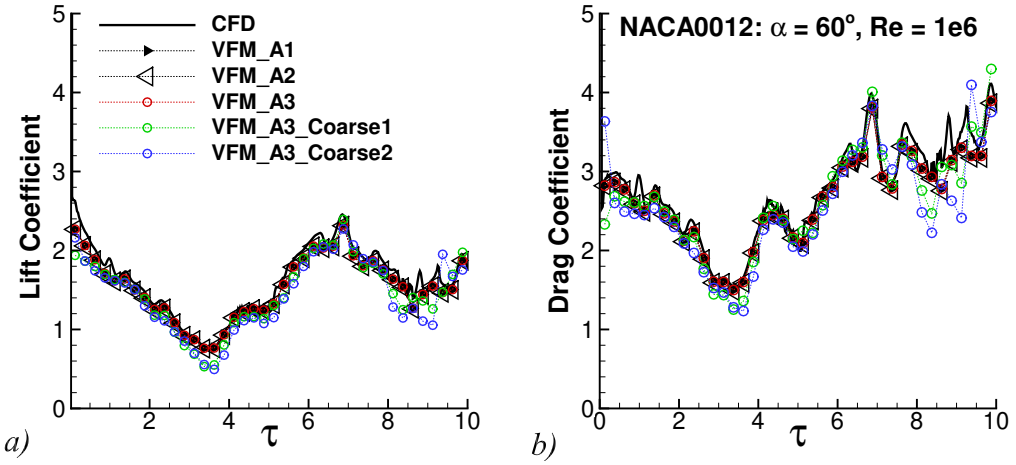

Fig. 12 Comparison of force coefficients from converged CFD results and from VFM method with different domain size and coarse sampling for NACA0012 airfoil at $Re = 1e6$.

Table 1 Relative Root Mean Square Error of Prediction

Cases	$A1$	$A2$	$A3$	$A3(Coarse1)$	$A3(Coarse2)$
$C_{L,Cylinder}$ (Ref. Fig. 11(a))	1.193%	1.013%	7.569%	15.57%	18.34%
$C_{D,Cylinder}$ (Ref. Fig. 11(b))	4.863%	4.906%	8.765%	7.301%	14.70%
$C_{L,NACA0012}$(Ref. Fig. 12(a))	5.908%	6.212%	7.391%	12.08%	15.37%
$C_{D,NACA0012}$(Ref. Fig. 12(b))	4.685%	5.244%	6.927%	8.402%	13.61%

V. Conclusions

In this paper, the VFM method for high Reynolds number flows reported in a previous work has been extended to general viscous flows around translating rigid bodies at a larger range of Reynolds numbers. The force acting on the body in a flow field has been decomposed into four components: added mass, vortex pressure, viscous pressure and skin friction.

The vortex pressure term in the extended VFM method is the corrected form of the force expression originally considered by Li & Wu (2018) [22]. It is contributed from vorticity in the flow field and represented as the scalar product of the vortex pressure force factor and the local flow velocity. According to the vortex pressure force factors derived from the viscous governing equation, an improved method to construct vortex pressure force maps was demonstrated, which ensures contributions vanish from vortices far away from the body. The vortex pressure force factors can be easily obtained by solving the Laplace equations. The viscous pressure and skin friction terms are corrections due to viscosity. They are contributed by the vorticity in the boundary layer close to the body surface and inversely proportional to Reynolds number.

The extended VFM method was applied to a circular cylinder and NACA0012 airfoil flows, and validated against CFD results. In all cases considered we found that the dominant force was the vortex pressure force, and when Reynolds number was large enough, the correction force terms due to viscosity could be ignored. The force oscillation behavior can be associated with the vortex flow patterns and vortex pressure force maps in the same way as in the previous work of Li & Wu (2018).

Additionally, we demonstrated the computation of vortex forces using coarsely sampled data on a small truncated domain, and found that the method produce acceptable accuracy, which facilitates its application to computing body forces from PIV data. The extension of this method to turbulent flows and its application to flow measurement (e.g. PIV) data will be studied in the future.

Appendix A: Derivation of the Expression for Extended VFM Method

The force acting on the body can be written as the sum of the pressure force and the skin-friction force [17]:

$$\overrightarrow{F} = \iint_{S_B} P\overrightarrow{n_B}dS + \mu \iint_{S_B} \overrightarrow{n_B} \times \overrightarrow{\omega}\, dS \tag{18}$$

The second term on the RHS is already in the form of a function of vorticity. For the first term, we can use the Lamb-Gromyko equation (3) and the condition (5) satisfied on the body surface to transform it into a function of the vorticity field.

Integrating the scalar product of $\nabla\phi_k$ and equation (3) over the whole control volume (i.e. $\iiint_\Omega \nabla\phi_k \bullet (1) d\Omega$), with the help of the incompressible continuity equation (2) and through a series of algebraic transformations and applying Green's theorem, with $\overrightarrow{U} = 0$ on the body surface and $\nabla\phi_k = 0$ at infinity, we have

$$\begin{aligned} -\iint_{S_B} P\nabla\phi_k \cdot \overrightarrow{n_B} dS &= \rho \iint_{S_B+S_\infty} \phi_k \frac{\partial \overrightarrow{U_B}}{\partial t} \bullet \overrightarrow{n}\, dS + \rho \iiint_\Omega \nabla\phi_k \bullet \left(\overrightarrow{\omega} \times \overrightarrow{U}\right) d\Omega \\ &\quad + \mu \iint_{S_B+S_\infty} \phi_k \left(\nabla \times \overrightarrow{\omega}\right) \bullet \overrightarrow{n}\, dS \end{aligned} \tag{19}$$

Substituting equation (5) into the left-hand term of equation (19), we have $-\iint_{S_B} P\nabla\phi_k \cdot \overrightarrow{n_B} dS = \iint_{S_B} P n_{B,k} dS$. The flow is undisturbed and irrotational at infinity, thus $\iint_{S_\infty} \phi_k \frac{\partial \overrightarrow{U_g}}{\partial t} \bullet \overrightarrow{n}\, dS = 0$ and $\mu \iint_{S_\infty} \phi_k \left(\nabla \times \overrightarrow{\omega}\right) \bullet \overrightarrow{n}\, dS = 0$. Therefore, equation (19) can be simplified into

$$\begin{aligned} \iint_{S_B} P n_{B,k} dS &= \rho \iint_{S_B} \phi_k \frac{\partial \overrightarrow{U_B}}{\partial t} \bullet \overrightarrow{n}\, dS + \rho \iiint_\Omega \nabla\phi_k \bullet \left(\overrightarrow{\omega} \times \overrightarrow{U}\right) d\Omega \\ &\quad + \mu \iint_{S_B} \phi_k \left(\nabla \times \overrightarrow{\omega}\right) \bullet \overrightarrow{n}\, dS \end{aligned} \tag{20}$$

Projecting the force equation (18) into the kth-direction and substituting equation (20) into it, we arrive at the force formula in the kth-direction in the form of a summation of four components: the added mass force $F_k^{(add)}$, the vortex pressure force $F_k^{(vp)}$ caused by the convection of existing vortices in the flow field, the viscous pressure force $F_k^{(vis-p)}$ caused by the diffusion of vorticity contacting the body surface, and the skin-friction force $F_k^{(vis-f)}$

$$\begin{cases} F_k = F_k^{(add)} + F_k^{(vp)} + F_k^{(vis-p)} + F_k^{(vis-f)} \\ F_k^{(add)} = \iint_{S_B} \phi_k \frac{d\overrightarrow{U_B}}{dt} \bullet \overrightarrow{n}\, dS \\ F_k^{(vp)} = \rho \iiint_\Omega \nabla\phi_k \bullet \left(\overrightarrow{\omega} \times \overrightarrow{U}\right) d\Omega \\ F_k^{(vis-p)} = \mu \iint_{S_B} \phi_k \left(\nabla \times \overrightarrow{\omega}\right) \bullet \overrightarrow{n_B} dS \\ F_i^{(vis-f)} = \mu \iint_{S_B} \overrightarrow{n_B} \times \overrightarrow{\omega} \bullet \overrightarrow{i}\, dS \end{cases} \tag{21}$$

In two-dimensional flow, we have $\nabla = \left(\frac{\partial}{\partial x}, \frac{\partial}{\partial y}, 0\right)$, $\overrightarrow{\omega} = (0, 0, \omega_z)$, and $\overrightarrow{U} = (u, v, 0)$. The force expression (21) can now be simplified into (6).

Acknowledgments

We are grateful for the engaging discussions with Prof. Zi-Niu Wu on this paper. This work has received funding from the European Union's Horizon 2020 research and innovation programme under the Marie Sklodowska-Curie grant agreement No.765579.

References

[1] ZHANG, J., "Footprints of a flapping wing." *Journal of Fluid Mechanics*, Vol. 818, 2017, pp. 1–4. https://doi.org/10.1017/jfm.2017.173.

[2] BIRCH, J. M., and DICKINSON, M. H., "Spanwise flow and the attachment of the leading-edge vortex on insect wings," *Nature*, Vol. 412, 2001, pp. 729–733. https://doi.org/10.1038/35089071.

[3] Cummins, C., Seale, M., Macente, A., Certini, D., Mastropaolo, E., Viola, I. M., and Nakayama, N., "A separated vortex ring underlies the flight of the dandelion." *Nature*, Vol. 562(7727), 2018, p. 414. https://doi.org/10.1038/s41586-018-0604-2.

[4] Filella, A., Nadal, F., Sire, C., Kanso, E., and Eloy, C., "Model of collective fish behavior with hydrodynamic interactions." *Physical Review Letters*, Vol. 120(19), 2018, p. 198101. https://doi.org/10.1103/PhysRevLett.120.198101.

[5] van Rees, W., Gazzola, M., and Koumoutsakos, P., "Optimal shapes for anguilliform swimmers at intermediate reynolds numbers." *Journal of Fluid Mechanics*, Vol. 722, 2013. https://doi.org/10.1017/jfm.2013.157.

[6] Ansari, S., Zbikowski, R., and Knowles, K., "Non-linear unsteady aerodynamic model for insect-like flapping hover. Part 2: Implementation and validation," *Journal of Aerospace Engineering*, Vol. 220, 2006, pp. 169–186. https://doi.org/10.1243/09544100JAERO50.

[7] Hesse, H., and Palacios, R., "Dynamic Load Alleviation in Wake Vortex Encounters." *Journal of Guidance, Control, and Dynamics*, Vol. 39, No. 4, 2016, pp. 801–813. https://doi.org/10.2514/1.g000715.

[8] Ramesh, K., Gopalarathnam, A., Granlund, K., Ol, M. V., and Edwards, J. R., "Discrete-vortex method with novel shedding criterion for unsteady aerofoil flows with intermittent leading-edge vortex shedding." *Journal of Fluid Mechanics*, Vol. 751, 2014, pp. 500–538. https://doi.org/10.1017/jfm.2014.297.

[9] Li, J., and Wu, Z. N., "Unsteady lift for the Wagner problem in the presence of additional leading/trailing edge vortices." *Journal of Fluid Mechanics*, Vol. 769, 2015, pp. 182–217. https://doi.org/10.1017/jfm.2015.118.

[10] Li, J., and Wu, Z. N., "A vortex force study for a flat plate at high angle of attack." *Journal of Fluid Mechanics*, Vol. 801, 2016, pp. 222–249. https://doi.org/10.1017/jfm.2016.349.

[11] Xia, X., and Mohseni, K., "Lift evaluation of a two-dimensional pitching flat plate." *Phys. Fluids*, Vol. 25, 2013, p. 091901. https://doi.org/10.1063/1.4819878.

[12] Devoria, A. C., Carr, Z. R., and Ringuette, M. J., "On calculating forces from the flow field with application to experimental volume data." *Journal of Fluid Mechanics*, Vol. 749, 2014, pp. 297–319. https://doi.org/10.1017/jfm.2014.237.

[13] Milne-Thomson, L. M., *Theoretical Hydrodynamics.*, Dover Books on Physics, Dover Publications, 2013. URL https://books.google.co.uk/books?id=YrTDAgAAQBAJ.

[14] Wu, J. C., "Theory for aerodynamic force and moment in viscous flows." *AIAA Journal*, Vol. 19, 1981, pp. 432–441. https://doi.org/10.2514/3.50966.

[15] Saffman, P. G., *Vortex Dynamics*, Cambridge Monographs on Mechanics, Cambridge University Press, 1993. https://doi.org/10.1017/CBO9780511624063.

[16] Noca, F., "On the evaluation of instantaneous fluid - dynamic forces on a bluff body." *GALCIT Report FM96-5*, 1996.

[17] Chang, C. C., "Potential flow and forces for incompressible viscous flow." *Proceedings of the Royal Society of London. Series A: Mathematical and Physical Sciences*, Vol. 437, No. 1901, 1992, pp. 517–525. https://doi.org/10.1098/rspa.1992.0077.

[18] Howe, M. S., "On the force and moment on a body in an incompressible fluid, with application to rigid bodies and bubbles at high Reynolds numbers." *Quarterly Journal of Mechanics and Applied Mathematics*, Vol. 48, 1995, pp. 401–425. https://doi.org/10.1093/qjmam/48.3.401.

[19] Graham, W. R., Pitt Ford, C. W., and Babinsky, H., "An impulse-based approach to estimating forces in unsteady flow." *Journal of Fluid Mechanics*, Vol. 815, 2017, pp. 60–76. https://doi.org/10.1017/jfm.2017.45.

[20] Kang, L. L., Liu, L. Q., Su, W. D., and Wu, J. Z., "Minimum-domain impulse theory for unsteady aerodynamic force." *Physics of Fluids*, Vol. 30, No. 1, 2018, p. 016107. https://doi.org/10.1063/1.5010008.

[21] Noca, F., Shiels, D., and Jeon, D., "Measuring instantaneous fluid dynamic forces on bodies, using only velocity fields and their derivatives." *Journal of Fluids and Structures*, Vol. 11, 1997, pp. 345–350. https://doi.org/10.1006/jfls.1997.0081.

[22] Li, J., and Wu, Z. N., "Vortex force map method for viscous flows of general airfoils." *Journal of Fluid Mechanics*, Vol. 836, 2018, pp. 145–166. https://doi.org/10.1017/jfm.2017.783.

[23] Zhou, Y., Alam, M. M., Yang, H. X., Guo, H., and Wood, D. H., "Fluid forces on a very low Reynolds number airfoil and their prediction," *International Journal of Heat and Fluid Flow*, Vol. 32, No. 1, 2011, pp. 329–339. https://doi.org/10.1016/j.ijheatfluidflow.2010.07.008.

[24] Ohtake, T., Nakae, Y., and Motohashi, T., "Nonlinearity of the Aerodynamic Characteristics of NACA0012 Aerofoil at Low Reynolds Numbers," *Journal of the Japan Society for Aeronautical and Space Sciences*, Vol. 55, No. 644, 2007, pp. 439–445. https://doi.org/10.2322/jjsass.55.439.

[25] Critzos, C. C., Heyson, H. H., and Boswinkle, R. W., "Aerodynamic characteristics of NACA 0012 airfoil section at angles of attack from 0^o to 180^o," *Technical Report for National Advisory Committee for Aeronautics, TN 3361*, 1955.